4-5-2013

Subsurface imaging of carbon nanotube networks in polymers with DC-biased multifrequency dynamic atomic force microscopy

Hank T. Thompson
Birck Nanotechnology Center, Purdue University, hthomps@purdue.edu

Fabienne Barroso-Bujans
Consejo Superior de Investigaciones Científicas (CSIC)

Julio Gomez Herrero
Autonomous University of Madrid

Ronald Reifenberger
Birck Nanotechnology Center, Purdue University, reifenbr@purdue.edu

Arvind Raman
Birck Nanotechnology Center, Purdue University, raman@purdue.edu

Subsurface imaging of carbon nanotube networks in polymers with DC-biased multifrequency dynamic atomic force microscopy

Subsurface imaging of carbon nanotube networks in polymers with DC-biased multifrequency dynamic atomic force microscopy

Hank T Thompson[1], Fabienne Barroso-Bujans[2,5], Julio Gomez Herrero[3], Ron Reifenberger[4] and Arvind Raman[1]

[1] Birck Nanotechnology Center and School of Mechanical Engineering, Purdue University, West Lafayette, IN 47904-2088, USA
[2] Instituto de Ciencia y Tecnologia de Polimeros, CSIC, Juan de la Cierva 3, E-28006, Madrid, Spain
[3] Universidad Autonoma de Madrid, Spain
[4] Birck Nanotechnology Center and Department of Physics, Purdue University, West Lafayette, IN 47904-2088, USA

E-mail: hthomps@purdue.edu

Abstract

The characterization of dispersion and connectivity of carbon nanotube (CNT) networks inside polymers is of great interest in polymer nanocomposites in new material systems, organic photovoltaics, and in electrodes for batteries and supercapacitors. We focus on a technique using amplitude modulation atomic force microscopy (AM-AFM) in the attractive regime of operation, using both single and dual mode excitation, which upon the application of a DC tip bias voltage allows, via the phase channel, the *in situ*, nanoscale, subsurface imaging of CNT networks dispersed in a polymer matrix at depths of 10–100 nm. We present an in-depth study of the origins of phase contrast in this technique and demonstrate that an electrical energy dissipation mechanism in the Coulomb attractive regime is key to the formation of the phase contrast which maps the spatial variations in the local capacitance and resistance due to the CNT network. We also note that dual frequency excitation can, under some conditions, improve the contrast for such samples. These methods open up the possibility for DC-biased amplitude modulation AFM to be used for mapping the variations in local capacitance and resistance in nanocomposites with conducting networks.

(Some figures may appear in colour only in the online journal)

1. Introduction

The manufacture of reliable polymer nanocomposites with enhanced electrical and mechanical properties requires relevant characterization tools, especially at the nanoscale. For example, carbon nanotube–polymer composites are known to improve exciton dissociation in photovoltaics at low doping, increase electron transfer and electrical conductivity, and have been reported to increase the thermal conductivity by 70% [1]. At the same time, the performance of nanocomposites in these applications depends on the ability to characterize and control CNT dispersion, CNT–matrix interfacial properties and CNT interconnectivity with sub-10 nm resolution. While optical microscopy is limited in resolution for such characterization, the electron beam in scanning electron microscopy (SEM)

and transmission electron microscopy (TEM) may damage polymer samples and the sample preparation is not suitable for all samples.

For the reasons mentioned, there has been interest in the use of atomic force microscopy (AFM) for the nanoscale characterization of polymer nanocomposites. AFM methods used to characterize such materials have included topography scans using contact and amplitude modulation, nanoindentation, phase contrast imaging to characterize the surface, scanning conductance microscopy (SCM), and tunneling AFM (TUNA) [2–5]. All of these techniques only measure the properties of the surface. However, characterizing CNT composites requires the ability to image CNT networks *beneath* the surface at depths of 10–100 nm.

A method for subsurface imaging of nanocomposites using dynamic AFM has been proposed recently [6, 3, 5, 7] which utilizes electrostatic force microscopy (EFM). The EFM method discussed is a quantitative two-pass imaging technique often used for electrostatic surface characterization and dielectric variation [8]. However, this two-pass method involves a lift-off distance Z_{offset} after having imaged the sample once in a tapping mode scan with an amplitude setpoint A_{sp}. As such, the second pass is performed at an actual height of $Z_{offset} + A_{sp}$, which is larger than if the material contrast is captured in the first scan alone. This offset distance tends to reduce the resolution of the material contrast when compared to single-pass methods.

In this work, we focus on a single-pass dynamic AFM technique that allows the subsurface characterization of CNT composites with high resolution up to depths of 50–100 nm. The method is based on the experimental observation that when a conducting AFM tip oscillates in the attractive regime over grounded thin films of such nanocomposites, the application of a DC tip bias voltage leads to a strong phase contrast, clearly identifying CNTs and their connectivity with high resolution. We use the terminology 'DC-biased amplitude modulated AFM' to describe this method. The experimental setup for this method is identical to the scanning polarization microscopy method developed by Salmeron and co-workers [9, 10] to study condensation and wetting on surfaces. In these works, the mechanism of phase contrast formation in DC-biased AM-AFM was ascribed to spatial variations in the capacitance of the cantilever–sample system caused by local variations in an effective dielectric constant. However, as we will demonstrate in this paper, the mechanism of image formation in CNT composites using this method has a very different physical basis and arises from Joule dissipation, which has been seen in other methods [11].

Here we utilize DC-biased amplitude modulated AFM in the attractive regime to understand the fundamentals of phase contrast image formation in carbon nanotube–polymer composites. In this regime of imaging the net interaction forces are attractive [12] to avoid possibly damaging the sample, short-circuiting from a direct contact between the tip and nanotube or inadvertent charging of the sample surface. In the attractive regime, in the absence of electrostatic forces or tip voltage bias, there is little phase contrast (dissipation contrast) over the sample when imaging with

AM-AFM [13]. We demonstrate through modeling and experiments the physical origin of phase contrast on CNT–polymer composites when applying a DC tip bias in AM-AFM. Two samples are studied: a 2D CNT network beneath a 40 nm spin-coated SEBS polymer layer and a 3D CNT network dispersed in the polymer blend and spun cast to a thickness of ∼40 nm. We also demonstrate the use of multifrequency AFM by simultaneously exciting two cantilever eigenmodes [13, 14] and find that under some conditions it is possible to increase phase contrast in the second mode for subsurface CNT detection.

2. Materials and methods

The two types of polymer–CNT composite samples used in this experiment consisted of CNTs and a poly(styrene-*b*-ethylene butylene-*b*-styrene) (SEBS) polymer blend on a Si substrate with a 1 nm native silicon oxide layer. The first sample (designated S1) consists of single-walled carbon nanotubes (SWCNT) with a diameter of ∼0.5–1 nm grown via chemical vapor deposition (CVD) such that the CNTs on the Si substrate create a two-dimensional (2D) network on the surface, on which a polymer layer is spun cast. The polymer blend consists of 6 g l^{-1} SEBS/toluene solution. A 20 μl droplet is adsorbed on the substrate by spin coating at 70 rps for 45 s. As a trial run, different thicknesses of the polymer layer, varying from 40 to 100 nm, were tested. Initial results concluded that subsurface imaging with reasonably small voltages could be performed for thicknesses less than 100 nm. The results presented here are from 40 nm thick samples.

The second type of sample (designated S2) combines double-walled carbon nanotubes (DWCNT) with the SEBS solution. DWCNTs were first dispersed in 6 g l^{-1} SEBS/toluene solution by stirring overnight, followed by sonication in an ultrasonic bath at 50 W for 5 min. This created a 3D network of DWCNTs within S2 as the nanotubes are dispersed within the polymer at various heights and unknown orientations. Figure 1(a) provides a graphical illustration of the sample types S1 and S2.

The implementation of DC-biased AM-AFM scanning experiments on these samples is shown in figure 1(b). An uncoated, highly doped Si cantilever is electrically biased with a DC voltage externally applied to the AFM nose cone and the sample is grounded. Initially the cantilever is excited at its first natural frequency. Prior to obtaining images for analysis, the sample to be studied is imaged to find a relatively flat location free from debris. Also during this preliminary stage, the second natural frequency is found for dual mode imaging along with the necessary control parameters.

Data were acquired with an Agilent 5500 AFM using the dynamic mode in the attractive regime. The operating regime used here is the attractive regime because the tip experiences a net attractive force during the oscillation cycle, minimizing tip–sample contact, which could short the junction formed between the DC-biased tip and an emergent CNT or inject excessive charge into the sample. The other operating regime is called the repulsive regime, where the tip experiences net
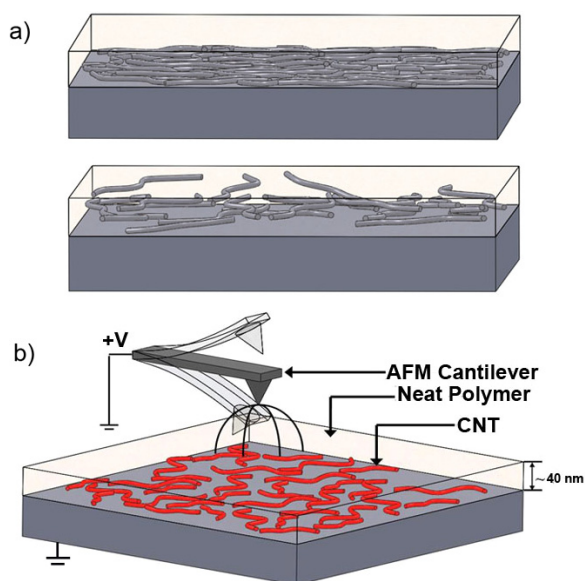
Figure 1. (a) Sample type schematic illustrating the differences between samples S1 and S2. The top schematic (S1) displays nanotubes in a 2D planar network, parallel to the substrate surface. The lower schematic (S2) illustrates the 3D network architecture with the nanotubes located at various depths and orientations. (b) Schematic of the single mode tip-biased amplitude modulation AFM experiment on sample S1. Here, the highly doped Si cantilever is electrically biased with an external DC voltage.
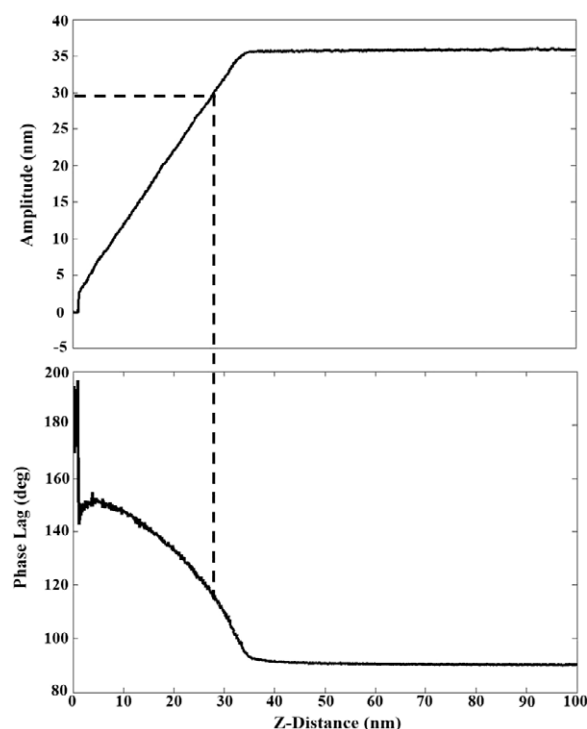

Figure 2. Characteristic amplitude and phase versus distance curve using the AppNano series cantilevers on sample S1. These plots highlight the fact that operating at an amplitude setpoint of 85% corresponds to an increase in phase lag. An increase in phase lag above 90° signifies imaging in the attractive regime.

repulsive interaction. These two regimes can co-exist even when the tip is excited at the natural frequency and the transition between the two can easily be influenced by the free amplitude, excitation frequency, and setpoint amplitude [12].

All experiments are performed with acoustic (dither-piezo) excitation. The lock-in amplifier is internal to the Agilent system software. The imaging regime is determined by performing dynamic force–distance (amplitude–distance) spectroscopy and measuring the phase lag at the setpoint amplitude. A phase lag in the fundamental mode above 90° indicates the attractive regime while the repulsive regime is denoted by a phase lag less than 90°. A characteristic fundamental mode amplitude and phase lag versus distance curve taken from the experiment with no applied bias voltage ($V = 0$) is found in figure 2, highlighting the fact that an amplitude setpoint of 85% corresponds to an increase in phase lag and imaging in the attractive regime.

Imaging was performed by using Applied Nanostructures FORT series and Olympus platinum coated AC240TM cantilevers. FORT cantilevers have a nominal stiffness of 3 N m^{-1} and the Olympus cantilevers have a nominal stiffness of 2 N m^{-1}. The single mode images on sample S1 were conducted using Olympus cantilevers and characterized by a resonant frequency of $f_0 \approx 80$ kHz, spring constant $k = 2.8$ N m^{-1}, quality factor $Q = 186$, and free amplitude $A_0 = 40$ nm. The Olympus cantilevers were excited at their resonant frequency ($f = 79.6$ kHz). The single mode images on sample S2 and the dual mode study on sample S1 were performed using the FORT cantilevers with a resonant frequency $f_0 \approx 60$ kHz, spring constant $k = 1.3$ N m^{-1}, quality factor $Q = 150$, and free amplitude $A_0 = 35$ nm. Sample S2 was imaged

at the FORT resonant frequency $f = 60$ kHz. The spring constant in all experiments was determined using Sader's method [15].

Dual mode operation also utilizes the second eigenmode of the cantilever, with an amplitude which is approximately 10% of that of the first mode free amplitude (387 kHz, 2.8 nm). The amplitude setpoint for imaging was 85%, based on the first mode amplitude. An important consideration for dual mode imaging is the initial phase assigned to the second mode resonance peak when no interaction forces are present. For the first mode of operation, one assumes that the phase lag is +90° when the drive frequency is tuned to resonance. However, the tip motion in the second eigenmode is opposite in phase to the part of the cantilever closest to the base. This is because the shape of the second eigenmode features a node across which the direction of oscillation reverses. At resonance, and before engaging the sample, the phase lag of the tip motion for the second eigenmode relative to the base is therefore −90°.

Data to be used for processing and analysis begins with single mode imaging without tip bias and the imaging setpoint remains constant. The bias voltage is increased by 0.5 V, and the area is imaged again. This procedure of increasing tip bias continues until the electrostatic force becomes too large and the subsurface CNTs become visible in the topography. Since we know that there are no surface CNTs in sample S1, this is an imaging artifact suggesting that the force gradient between tip and sample is now large enough to cause the Z-piezo to adjust as though there is a surface CNT present.
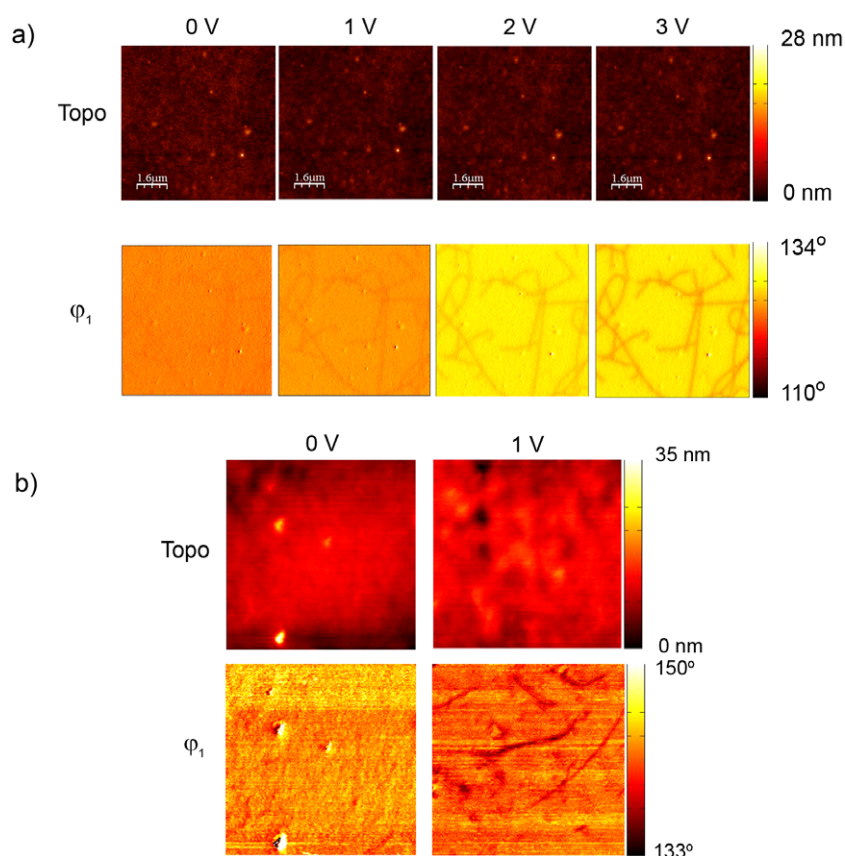
Figure 3. (a) Single mode results for sample S1. The top row is the AFM topography image and the bottom row contains the corresponding phase lag image. The 0 V image is the leftmost column. Moving left-to-right, the tip bias voltage is increased and, although the topography remains the same, the phase contrast between the subsurface CNTs and surrounding polymer becomes increasingly pronounced. (b) Topographical and phase lag results for sample S2. A distinguishable feature from the results in (a) is that, as the voltage increases, the contrast varies between different features. This difference in phase contrast is believed to be due to the various CNT heights and different electrical interactions between tip and sample.

Once this point is reached, the tip bias voltage is cycled back to zero and the system's dual mode feature is activated. The specifics of dual mode imaging can be found in [14, 13]. It is important to reiterate that the two additional information channels, the amplitude and phase of the second eigenmode, are free to change and thus provide two additional material property contrast channels. The imaging procedure from before is followed again, starting with no bias voltage applied and increasing until artifacts are found within the topography image. To be consistent, the same procedure is followed when imaging either sample type (S1, S2).

Image post-processing converting the phase lag images to the virial and dissipation was performed using the WSXM software [16]. Image processing was done using WSXM and MATLAB (MathWorks, Inc.) software.

3. Experimental results

3.1. Single mode DC-biased AFM results

Figure 3(a) shows the single mode results for sample S1. The top row is the AFM topography image and the bottom row contains the corresponding phase lag image. The 0 V image is the leftmost column. The topography does not indicate any great abnormality or asperity and there is little to no phase contrast in the phase lag image. Moving left-to-right, the tip bias voltage is increased and, although the topography remains the same, the phase contrast between the subsurface CNTs (40 nm below surface) and surrounding polymer becomes increasingly pronounced. Although the CNTs have a diameter of <1 nm, they appear to have a much larger diameter in the phase lag image. This is expected since the measured phase lag image convolves the long-range electric field between the tip and the sample with the actual subsurface object.

The topographical and phase lag results for sample S2 are found in figure 3(b). As before, the 0 V image is presented first, followed by one incremental voltage image. The most interesting detail from this result is that not only is there a differing extent of the phase contrast from CNT to CNT, but also within the same CNT it is possible to observe a change in the phase contrast along the CNT length. This is in contrast to the results for sample S1, where we found that the nanotubes have a nearly equal contrast along their length and all of the nanotubes within the image appear similar. We believe this difference in phase contrast is due to the differing CNT orientations and depths relative to the sample plane.

At this point it is interesting to consider if, in fact, the phase contrast images observed could be due to an artifact of the single-pass imaging method. For example, if the CNTs lay on the surface, a single-pass DC-biased EFM method would not correctly account for the CNT topography, in which case the two-pass method would be appropriate. However, it is important to note that in the 2D sample (S1), the single-walled CNTs are buried far beneath the free surface of the film so that the top surface topography should not contain any CNT features. This can be seen in figure 3(a), where the topography of the sample does not indicate the CNTs. This conclusion could be problematic for sample S2, where surface or near-surface CNTs may be located. In the samples we have imaged, however, we do not see CNTs in the topography image (figure 3(b)) and have found that when CNT composite samples are well prepared and spun cast on a hard substrate, the CNTs do not usually emerge from the surface. While some CNTs must lie near the surface, we account for this since we image in the attractive regime with little tip–sample contact. By imaging in this regime, the measured topography does not indicate the presence of near-surface CNTs unless a large tip bias is applied. As a result, single-pass imaging is sufficient for these samples.

3.2. Dual mode DC-biased AFM results

The imaging results using the dual mode method on sample S1 are found in figure 4(a). Here, the far-left column corresponds to the 1 V images, and the applied bias voltage increases moving to the right. The new row of images is associated with the additional information obtained with dual mode. This information channel corresponds to the phase of the second, or additional, eigenmode being excited.

Since dual mode imaging captures both the first and second eigenmode phase, it is necessary to plot them on the same absolute range in order to make a fair comparison. In figure 4(a) with an equal absolute range for ϕ_1 and ϕ_2 (45°), looking at the 2 and 2.5 V result in particular, one can see that the second eigenmode phase provides more absolute contrast and thus greater sensitivity, however, the noise has also increased, at least under the imaging conditions explored in this work. We explore both of these issues in more detail now.

Bimodal imaging has previously been used to increase force sensitivity as compared to single mode imaging [13, 17–20]. To quantify this improved sensitivity for our samples, we considered the average of the values of ϕ_1 and ϕ_2 over ≈80 pixels on a fixed area covering the CNT and another area of equal size of neat polymer using the WSXM software [16]. The absolute difference of these average values of phase on the CNT and on the neat polymer ($\phi_{CNT} - \phi_{poly}$) was evaluated for each mode as a function of the different values of applied tip bias voltage. The results of this study are given in figure 4(b). The phase contrast between CNT and polymer is ≈10 times greater for the second mode compared to the first mode. Moreover, it is easy to see that the first mode has a gentle, linear slope while the second mode has a much more aggressive, higher-order behavior with respect to the applied voltage.

As we have seen, this increased sensitivity in bimodal operation, at least under our experimental conditions, is accompanied by a decrease in signal to noise in the second mode phase image. The second mode phase images shown have been acquired after optimizing the time constants of the internal lock-in amplifiers to reduce noise in the second mode phase image. Using dual mode imaging, the nature of cantilever oscillations when interacting with the sample leads to the fact that the tip motion has a long fundamental time period [21]. Often, this time period is beyond the lock-in time constant, so that within the lock-in time constants used the motion may not have been very periodic. We believe that this results in the observed noise in phase.

4. Theory

The results above clearly demonstrate that subsurface single-walled carbon nanotubes can be clearly observed in the phase contrast image when a tip bias is activated, in both samples S1 and S2, but also raise some fundamental questions: what is the origin of phase contrast in these samples? Why does dual mode operation provide greater phase contrast? In order to understand and answer these questions, a theoretical basis for the results from these experiments must be developed.

At first it might seem, as suggested by Salmeron and co-workers [10, 22], that the phase contrast in single mode operation appears as a result of local variations in the effective dielectric constant or polarization of the sample which would effectively change the local capacitance from point to point on the sample. In this theoretical explanation, the electrostatic force between the tip and sample would depend on the local effective dielectric constant as follows:

$$F(d) = -4\pi\varepsilon_0 \frac{\varepsilon - 1}{\varepsilon + 1} \frac{R_{tip}^2}{d^2} V_{tip}^2 \tag{1}$$

where ε is the local dielectric constant, d the tip–sample distance, R_{tip} the tip radius, and V_{tip} the applied bias voltage [23]. According to Zhao *et al*, the effect of a nanotube within the probing volume of the sample is to modify the local effective dielectric constant, which in turn changes the local electrostatic forces and gradients. Changing electrostatic force gradients could detune the cantilever resonance, leading to phase shifts.

However, the theory of amplitude modulated AFM clearly shows that the phase lag ϕ and the amplitude reduction (when driving at resonance) are given by [24]

$$\sin(\phi) = \left[\frac{Q}{\pi k A A_0} E_{diss} + \frac{A}{A_0} \right] \tag{2}$$

$$\cos(\phi) = -\frac{2Q}{k A A_0} \langle F_{ts} \cdot q(t) \rangle \tag{3}$$

$$\frac{A}{A_0} = \frac{1}{\sqrt{[1 - \frac{Q E_{diss}}{\pi k A^2}]^2 + [\frac{2Q}{k A^2} \langle F_{ts} \cdot q \rangle]}} \tag{4}$$
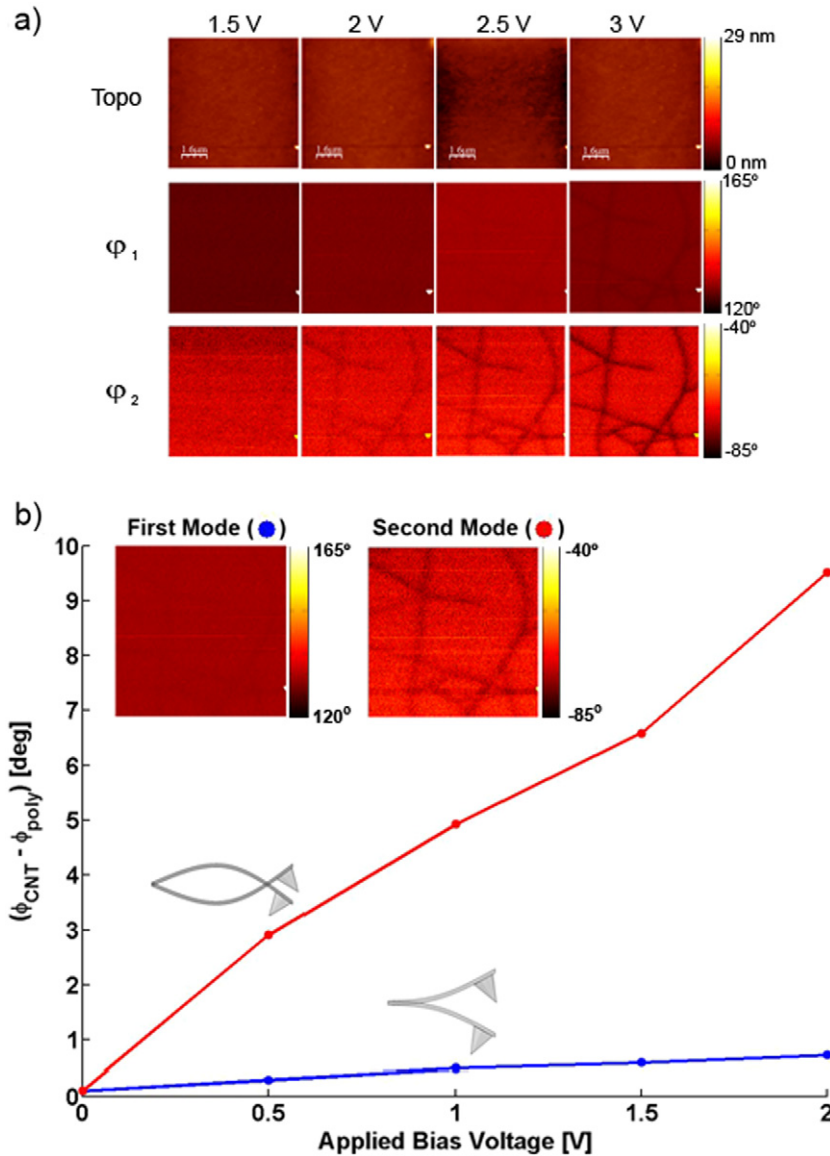
Figure 4. (a) Dual mode results on sample S1. The far-left column corresponds to the 1 V images and the applied bias voltage increases moving to the right. A new row of images are included, and these images are the phase lag of the second eigenmode being excited. To allow for a fair comparison between the phase lag images of the first and second eigenmodes, they are plotted on the same absolute range (45°). It is important to recall that the phase lag in the first eigenmode begins at 90° while the second eigenmode phase lag begins at −90°.
(b) Results of the sensitivity study to look at the proposed increase between the first and second eigenmode phase channel. In this study, one area of SWCNT and one area of neat polymer, each of equal size, were captured at the same location for each phase image. A histogram analysis was performed on each area and for each mode (ϕ_1, ϕ_2). The average value found for polymer was subtracted from the average for CNT. From the results, it is easy to see the linear, gentle slope for the first eigenmode and the more aggressive, higher-order behavior of the second eigenmode. However, the signal to noise ratio in the second mode has decreased appreciably in this case.

where A is the setpoint amplitude, A_0 the free amplitude, Q the quality factor, k the cantilever spring constant, and $E_{\mathrm{diss}} = \int_0^T \dot{q}(t) \times F_{\mathrm{ts}} \, \mathrm{d}t$ the dissipated energy during the tip–sample interaction. The expression for $\cos(\phi)$ is in terms of the quantity $\langle F_{\mathrm{ts}} \cdot \dot{q}(t) \rangle = \frac{1}{T} \int_0^T \dot{q}(t) \times F_{\mathrm{ts}} \, \mathrm{d}t$, where T is the time period of oscillation. This quantity is also called 'the virial' of the tip–sample force and measures the conservative part of the tip–sample energy stored and released as the tip position $q(t)$ oscillates harmonically with respect to the sample at a height Z above the sample as in figure 6.

In particular, these formulas clearly show that the amplitude reduction (equation (4)) is due to both conservative and dissipative effects and the AFM adjusts the height Z at each point on the sample to keep the amplitude ratio (setpoint) constant. In doing so, it is very important to note that the virial and dissipation are then intrinsically related through equation (4) and are not independent quantities.

These formulas are equally valid for both long and short range forces. Since the setpoint amplitude is held constant, equation (4) clearly shows that contrast in virial alone cannot result in phase contrast but rather one must have a dissipation
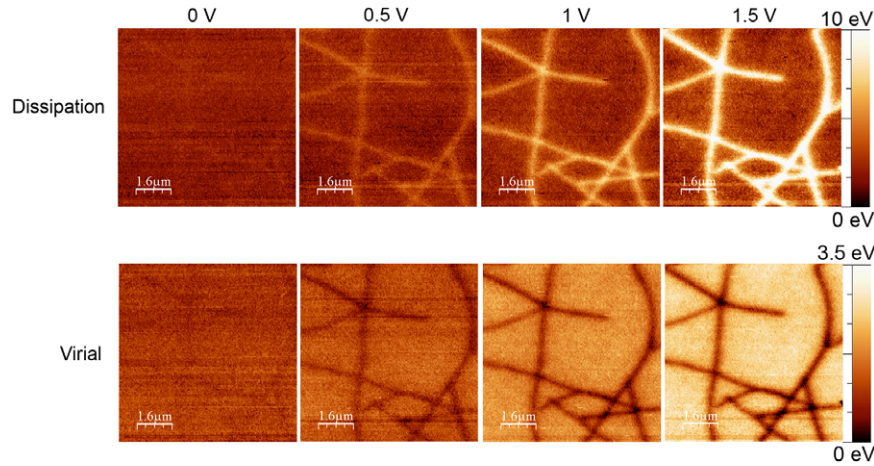
Figure 5. Virial and dissipation maps needed to verify the theoretical result that dissipation must be involved to provide phase contrast in AM-AFM. These maps were created using phase lag images obtained in single mode on sample S1.

mechanism active even in the attractive regime of operation. Taking the extreme case where there is no dissipation, $E_{diss} = 0$, there must be no phase contrast since $\sin(\phi) = \frac{A}{A_0}$ and contrasts in conservative interactions alone cannot create the observed phase contrast. Rather, in tapping mode AFM the virial and dissipation are inherently linked, which implies that some contrast in energy dissipation must accompany any expected contrast in conservative electrostatic forces (i.e. dielectric constant, van der Waals, etc) Moreover, this dissipation acts even when the tip oscillates in the attractive regime and there is greater dissipation over the CNTs than on the neat polymer.

To verify this theoretical result we use the following expressions for the virial and energy dissipation

$$\langle F_{ts} \cdot q(t) \rangle = -\frac{kAA_0}{2Q} \cos(\phi) \qquad (5)$$

$$E_{diss} = \frac{\pi kAA_0}{Q} \left[\sin(\phi) - \frac{A}{A_0} \right] \qquad (6)$$

to use the observables to convert into maps of virial and dissipation in the scan. Single mode phase lag contrast images obtained on sample S1 were converted to the virial and energy dissipation using equations (5) and (6) and the resulting maps are shown in figure 5.

Figure 5 clearly shows that there is contrast in both dissipation and virial when the tip oscillates over the CNT as compared to on the neat polymer. In particular the energy dissipation over the buried CNT is greater than on the neat polymer. This raises two key questions. What is the source of energy dissipation triggered when the tip is oscillating in the attractive regime? Why is the dissipation larger when the DC-biased tip oscillates over a buried carbon nanotube in the attractive regime of operation? To answer these questions, an electromechanical model of the system was developed that identified the source of this measured dissipation.

Before discussing the mathematical model, it is important to consider the physics to be modeled. The physics of electromechanical dissipation is identical to the one suggested by Denk and Pohl [11]. Namely, upon application of a DC

voltage and oscillating tip, the capacitance is modulated through the cantilever oscillation, which creates an oscillation current in the cantilever–sample equivalent circuit and dissipates in Joule heating. If the grounded sample is a lossless dielectric or perfect conductor, then the electrostatic forces would be conservative and no electrical dissipation would occur. When this is not the case then the variation of surface charge due to cantilever oscillation leads to electrical dissipation. In other words the surface charge induced by cantilever oscillation on the sample dissipates at its own characteristic timescale of the RC circuit representing the local resistance and capacitance of the nanocomposite. This energy dissipated in the local electrical circuit of the sample must arise from two sources, namely the mechanical motion of the cantilever, which modulates the capacitance of the air gap, and the electrical source of the DC bias, which maintains a constant voltage in the presence of a changing capacitance.

Figure 6(a) provides a graphical illustration of this model, where V_0 is the bias voltage applied to the tip, $V(t)$ is the time-varying voltage induced on the sample surface, and the sample is grounded on the bottom side. $C_{air}, \varepsilon_{air}$ are the capacitance and dielectric constant of ambient air and $C_{sample}, \varepsilon_{sample}, R_{sample}$ represent the effective local capacitance, local dielectric constant, and local resistance of the sample. By 'local' it is meant that these are effective values over the probed volume of the sample that experiences significant time-varying electric fields from the oscillating tip. These local values change spatially across the sample depending on the location and distribution of nanotubes in the probed volume. Z and $q(t)$ are the distance to the undeflected cantilever tip and the tip deflection from the undeflected position, respectively.

This model is a tool to understand the mechanism by which energy is dissipated in this system. A plane surface estimation [25] is used to model the system and is applicable in the case of a large tip. A much more thorough, but extremely complex model, would include the spherical tip, cone apex, and rectangular contributions, similar to other models proposed in [25]. However, we find that our
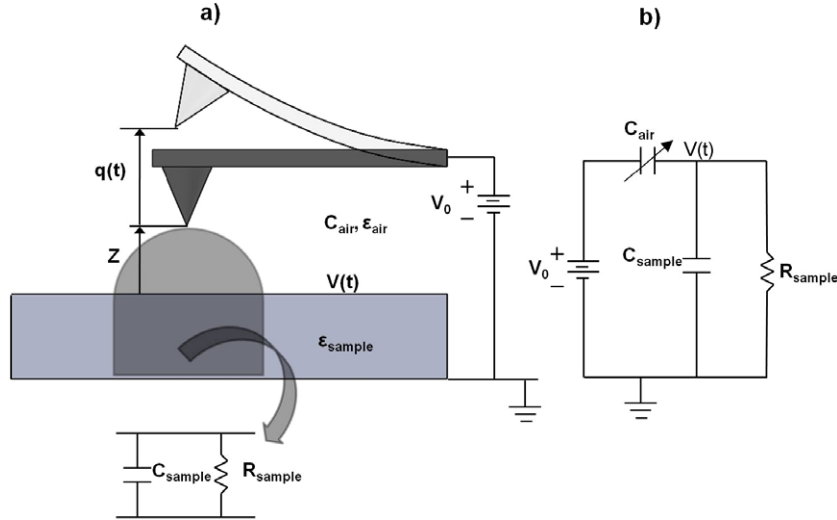
Figure 6. Electromechanical model of the AFM tip and sample system to identify the source of measured dissipation. (a) V_0 is the bias voltage applied to the tip, $V(t)$ is the time-varying voltage of interest between the tip and sample, and C_{air}, ε_{air} are used to describe the capacitance and dielectric constant of ambient air. C_{sample}, ε_{sample}, R_{sample} represent the effective local capacitance, local dielectric constant, and local resistance of the sample. Local here implies that these values can change spatially across the sample. Z and $q(t)$ are the distance to the undeflected cantilever tip and the tip deflection, respectively. (b) is the equivalent circuit of the model. The cantilever is electrically biased and oscillates, thus the capacitor C_{air} varies with time.

assumption is in reasonable agreement and the dissipation is of the same order of magnitude as that found in the experiment.

　　Figure 6(b) is the equivalent circuit of the proposed model. The cantilever is electrically biased and oscillates, therefore the corresponding capacitance C_{air} varies with time. Within the model we have assumed that the cantilever tip motion is known and prescribed to be sinusoidal, which is a reasonable assumption for operation in the attractive regime.

　　The equations governing this equivalent circuit model are:

$$C_{air}(t) = \frac{\varepsilon_{air}A_{tip}}{(Z + q(t))} \tag{7}$$

$$C_{sample} = \frac{\varepsilon_{sample}A_{tip}}{t_{sample}} \tag{8}$$

$$\frac{d}{dt}(V(t)) = -\frac{1}{\left(C_{sample} + C_{air}(t)\right)}$$

$$\times \left[V(t)\left(\frac{1}{R_{sample}} + \frac{d}{dt}(C_{air}(t)) \right) - V_0\frac{d}{dt}(C_{air}(t)) \right] \tag{9}$$

$$F = -\frac{1}{2}\left[\frac{dC_{air}(t)}{dq(t)}(V_0 - V(t))^2 \right] \tag{10}$$

where A_{tip} is the area of a large radius tip $\left(\pi r^2 \right)$, and is the area necessary for the assumed parallel plate model, and t_{sample} is the thickness of the sample, including both the polymer and native oxide layer on Si (≈ 40 nm) [26]. The cantilever–sample interaction force F is described as the change in potential energy with respect to the changing gap of the capacitor. Deriving analytical solutions to this system of coupled equations is not feasible and we resort to the specialized Cadence software, PSpice [Cadence SPB 16.01].

　　With the desired voltage output of the model $V(t)$, equation (10) was used to determine the force experienced by the cantilever during an oscillation cycle. The nominal values used for this simulation are: $Z = 30$ nm, $q(t) = 27$ nm $\cdot \sin(\omega \cdot t)$, $\omega = 60$ kHz, and $V_0 = 3$ V. Calculating the force on the cantilever F, the tip–sample distance d is determined from $d = Z + q(t)$. In this simulation, C_{sample} was calculated assuming the plane surface model [25] with a tip radius of 50 nm, polymer thickness $t_{sample} = 40$ nm, and dielectric constant estimated to be 2.7 [27]. R_{sample} was varied depending on two cases. The first case considers the possibility where the local sample resistance is very large and approximates an infinite resistance situation, say 1 PΩ (10^{15} Ω). Performing this simulation, it is found in figure 7 that as one plots the force versus tip–sample separation during one cycle of oscillation that there is negligible energy dissipation. As described earlier, without energy dissipation there can be no phase contrast.

　　It is interesting to note that the electrostatic force magnitude with a total sample resistance of 1 PΩ is much smaller than the magnitude with a 1 GΩ resistance. This is because the electrostatic force magnitude scales as the square of the voltage difference between the cantilever and the voltage developed on the sample surface (equation (10)). At large sample resistance, little current flows through the sample, thus resulting in a negligible voltage drop between the cantilever and sample surface and a reduced electrostatic force.

　　Next, the local sample resistance is allowed to be finite, 1 GΩ [27]. This represents the resistance of a thin layer of SEBS polymer with a percolating network of carbon nanotubes inside. Performing the simulation, one can see in figure 7 that a hysteresis loop forms between the approach and retraction during one cycle of oscillation.
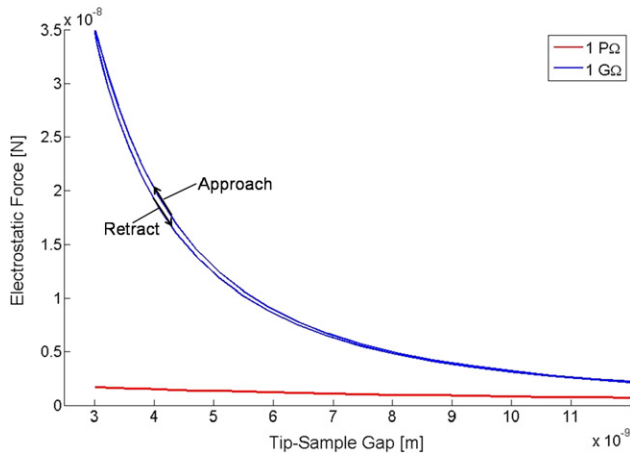
Figure 7. Simulation results comparing the two sample resistance situations. The finite resistance was chosen to be 1 GΩ, whereas the much larger, approaching infinite resistance value was 1 PΩ. Clearly, the hysteresis in the 1 GΩ force plot demonstrates that energy is being dissipated. Conversely, when plotted on the same scale, the approach and retract curves lie on top of one another in the approaching infinite resistance case, meaning that very little to no energy is dissipated. The labeled arrows denote the corresponding direction of the cantilever motion with respect to the sample.

Figure 8. Simulation results varying the capacitance of the sample. There is a dependence of energy dissipation on the local dielectric of the sample. From this plot, it is found that the dielectric constant of the sample decreases and there is an increase in energy dissipated.

Voltage-dependent noncontact dissipation has been studied with AFM in previous literature [11, 28] and, as stated earlier, is attributed to electrical Joule dissipation [29]. Additionally, this electromechanical dissipation mechanism is closely related to the idea of capacitive braking described in capacitive micromechanical switches for radio frequency (RF) communications applications [30]. In conclusion, a basic electromechanical model was created that identified the source of DC-biased energy dissipation in the nanocomposite as being due to induced current dissipation in the CNT composite to ground circuit.

We have also performed additional experiments on highly ordered pyrolytic graphite (HOPG) samples with an external resistor. These results are described in the appendix and clearly demonstrate how the energy dissipation changes when the external resistor is changed, clearly demonstrating the presence of this electromechanical dissipation mechanism.

To explore this model further, the capacitance of the sample is varied and it is found that there is an explicit dependence of energy dissipation on the local dielectric constant of the sample as well. The results for this comparison are found in figure 8. Here it is found that as the dielectric constant of the sample decreases, there is an increase in energy dissipation. This is attributed to the reactance of the sample, determined by the capacitance ($Z \propto \frac{1}{C}$). As the capacitance decreases, the reactance increases and the division of current between the sample capacitor and resistor varies. With increasing reactance, more charge flows through the resistor and results in larger dissipation. From this study one can see that energy dissipation in DC-biased amplitude modulation AFM maps a combination of local spatial changes in the capacitance and resistance of the medium.

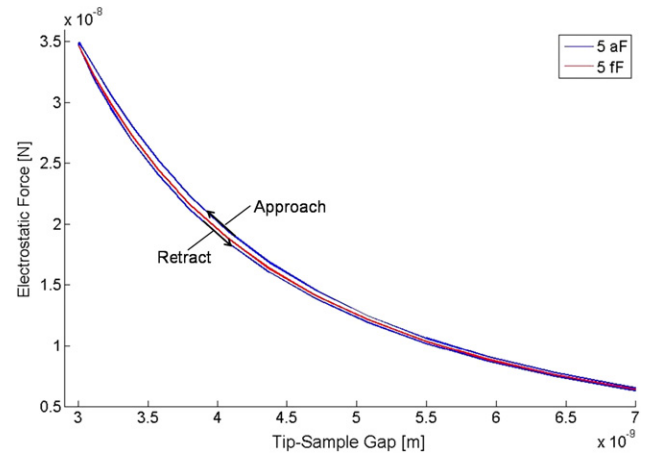Having discussed the origin of phase contrast in single mode operation we move to discussing the results on dual

mode imaging described in figure 4(a). This is motivated by exploring other eigenmodes that could allow the imaging of buried CNTs at lower DC tip bias voltages. In dual mode AFM, the amplitude of the first eigenmode is used to track the topography while the second eigenmode amplitude and phase shift are used as complementary channels to explore the tip–surface forces. Studies in dual mode AFM have shown that there is a marked increase in force sensitivity and phase contrast to detect mechanical and electrical interactions [13, 14].

The importance of dual mode operation in this setting arises from the fact that DC-biased imaging is performed in the attractive regime of tip–sample interaction. In the absence of the electromechanical dissipation, there is likely to be little contrast in the phase of the fundamental eigenmode. However, as has been shown by [20], one can measure phase contrast in the second eigenmode even in the attractive regime. This is because the phase of the second eigenmode is sensitive to both conservative and dissipative interactions. Thus the use of the bimodal scheme is expected to boost the phase contrast.

In order to better understand the mechanism of contrast improvement in the bimodal scheme for this sample, dual mode dynamic force spectroscopy studies were performed in VEDA, an AFM simulation tool (http://nanohub.org/resources/veda), under the advanced approach curves option. In an attempt to keep the parameters as close to the actual environment as possible, we chose the following for the first eigenmode: $f_0 = 60$ kHz, $k = 1.3$ N m^{-1}, $Q = 150$, $A_0 = 35$ nm, and for the second eigenmode: $f_2 = 387$ kHz, $Q = 330$, and $A_2 = 2.8$ nm.

The electrostatic tip–sample interaction model of Xu and Salmeron [22] for sphere-plane was used for this simulation. In contrast to the previous model (figure 6(a)) which used a coarse approximation for electrostatic forces but included a current leakage model, the Xu and Salmeron model is a better representation of the electrostatic forces but does not include the leakage current/Joule dissipation effect. In this simulation, the sample's dielectric constant is varied by one
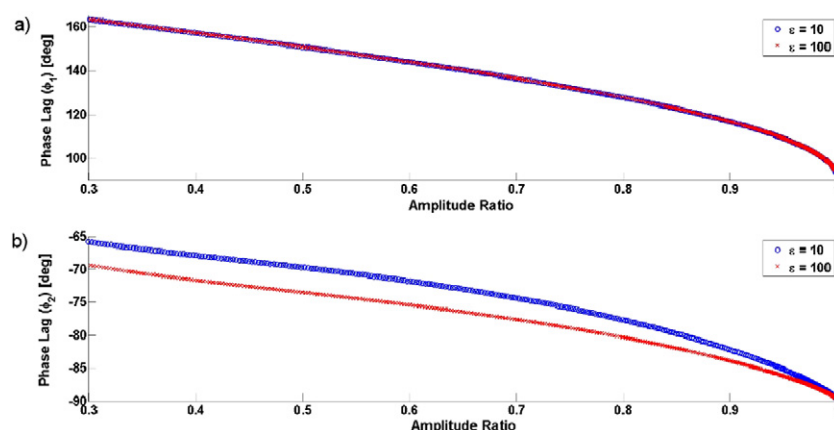
Figure 9. VEDA dynamic force spectroscopy simulation results for dual mode operation comparing the influence of dielectric constant ($\varepsilon = 10 - 100$) on first mode and second mode phase lag, applying a fixed DC bias voltage of 1 V. (a) First mode phase lag results showing no change for varying dielectric constant. (b) Second mode phase lag showing marked change, thus validating the increased sensitivity and contrast for conservative interactions.

order of magnitude ($\varepsilon = 10 - 100$), but the applied DC bias voltage is held fixed at 1 V.

The simulation results are provided in figure 9. Figure 9(a) presents the phase lag of the fundamental mode from varying dielectric constant as a function of amplitude setpoint ratio. It is clear that there is no change between the two separate cases and the phase lag results lie on top of one another. Dual mode phase lag results are found in figure 9(b), and there is a marked difference for the two cases as a function of amplitude setpoint ratio of the fundamental eigenmode. In both plots, the data is presented for an amplitude ratio of 30%.

This simple simulation shows that even in the absence of electromechanical dissipation, the second mode would in fact show a phase contrast due to changes in local dielectric constants, whereas the phase of the fundamental mode would not show a contrast since there is no change in dissipation. When electromechanical dissipation is included the phase contrast on the second mode is only expected to increase further. Thus the improved sensitivity of the second mode phase is clarified. However, as mentioned before, this improvement depends on a number of factors, such as the amplitude ratio of the first and second eigenmodes and choice of the appropriate time constants in the two lock-in amplifiers.

5. Practical considerations that affect the DC-biased AFM method

The method described here for subsurface imaging has been used on samples which are well characterized and designed for this analysis. However, not all samples will show subsurface features in the phase image in single pass, DC-biased AFM even in the presence of a bias voltage.

This mechanism is observable for significant capacitance modulation of the cantilever–air–sample capacitor. If the film's thickness is large (>100 nm) compared to the oscillation amplitude, then the capacitance modulation is small and the subsurface CNTs are difficult to visualize in the phase contrast even at large voltages. When imaging thick films, we have found that placing an electrode on the top

surface near the imaging area improves imaging of near-surface CNTs. In this situation, the cantilever–air–sample capacitance is decreased and the cantilever oscillation can create a significant capacitance fluctuation.

The depth at which imaging is possible depends on the penetration depth of the electric field into the sample. This depth resolution is influenced by the applied bias voltage; increasing this voltage decreases the spatial resolution in that the features become blurred. Conversely, decreasing the bias voltage for better spatial resolution leads to a reduction in the imaging depth.

6. Conclusions

In conclusion, the use of DC-biased amplitude modulation atomic force microscopy (AFM) was studied in the attractive regime using both single and dual mode excitation, which allowed the *in situ*, nanoscale, subsurface imaging of single- and double-walled CNT networks dispersed in a polymer matrix at depths of $\approx$10–100 nm. The mechanisms for image formation in the fundamental phase have been studied using theoretical models which clearly identify the existence of an electromechanical dissipation mechanism active in the attractive regime of the tip–sample interaction. It is also found that the use of dual mode imaging can, under certain operating conditions, provide better sensitivity to subsurface CNTs in DC-biased AFM, albeit in our experiments these images are accompanied by greater noise.

We expect that DC-biased imaging of subsurface CNT networks will be an attractive option when extra lock-in amplifiers are not available or when two-pass methods compromise the desired resolution. Given the increasing interest in polymer nanocomposites with nanophase filler materials, we expect that this technique, along with the two-pass EFM method and Kelvin probe force microscopy, will become increasingly popular. However, a thorough comparative study of these techniques is needed to understand better their limitations and benefits with respect to these samples. This remains a subject of ongoing research.
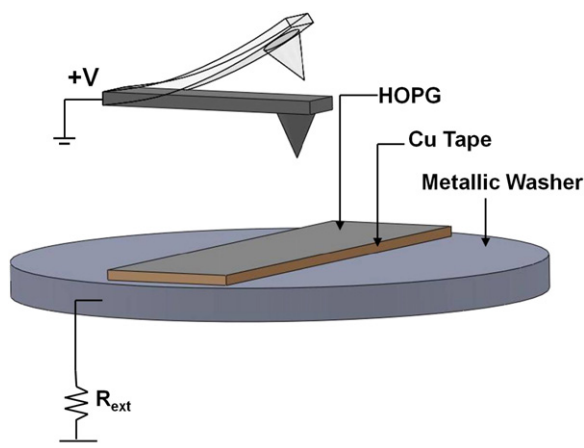
Figure A.1. Schematic of dynamic force spectroscopy experiment on grounded HOPG with an external resistor. This was a study to determine the significance of external resistance on energy dissipation.

Figure A.2. Results from fixed DC bias voltage study and varying external resistance, R_{ext}. This result clearly indicates that the energy dissipated increases with increasing external resistance.

Figure A.3. Additional PSpice simulations to determine resistance behavior on energy dissipation.

Appendix

Here we provide an additional study we have performed to confirm and understand the unique electromechanical dissipation model presented in the main text. In this study, we investigate electromechanical dissipation on highly ordered pyrolytic graphite (HOPG) with external resistors. If the underlying dissipation mechanism is indeed the electromechanical model that we have presented, then the measured energy dissipation should depend on the choice of external resistor. On the other hand, if the dissipation mechanism is not the one discussed in this paper, then the energy dissipated should be independent of the choice of external resistor. We used an experimental setup similar to that for the subsurface imaging technique to determine the importance of resistance in this experiment. Figure A.1 is a schematic illustrating the experiment performed. We have accomplished our goal by including an external resistor between the sample and ground and performed dynamic force spectroscopy on freshly cleaved HOPG. The cantilever used for this study is an AppNano FORT series silicon cantilever with resonance frequency $f_0 = 60$ kHz, quality factor $Q = 130$, spring constant $k = 1.9$ N m^{-1}, and free amplitude $A_0 = 18$ nm. The cantilever was driven at its resonance frequency and made to approach the sample. The spectroscopy curves were then processed by applying equation (6) to convert the data into energy dissipation as a function of amplitude setpoint ratio.
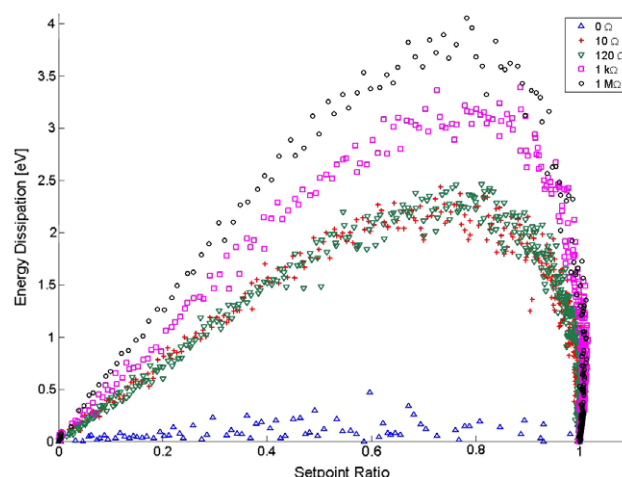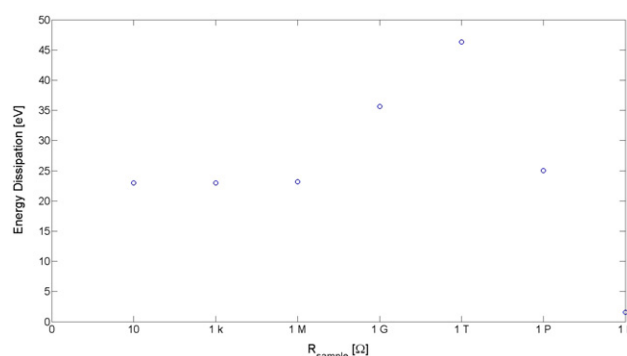
This study was run by fixing a DC bias voltage applied to the cantilever and varying the external resistor value from 0 Ω to 1 MΩ. Next, the DC bias was increased and the resistor study performed again at the new cantilever voltage. Figure A.2 represents the results for the 2 V DC bias voltage study. The trend is clear in showing that the dissipated energy increases with increasing external resistance. At extremely high resistor values, we should again expect a reduction in energy dissipated. This study confirms the electromechanical dissipation mechanism that we have discussed earlier in the manuscript.

We have also performed additional simulations using the PSpice software to study the energy dissipation behavior with increasing resistance. We were mainly interested in finding out if there is a resistance which offers maximum dissipation and if increasing the resistance further would decrease the dissipation (as the experiment suggests). Using the same simulation parameters as before in figure 7, we are able to vary the resistor values on a much larger scale. As we expected, the results in figure A.3 indicate that there is a resistance which offers maximum dissipation and larger resistances cause a rapid decrease.

References

[1] Landi B J, Raffaelle R P, Castro S L and Bailey S G 2005 Single-wall carbon nanotube–polymer solar cells *Prog. Photovolt. Res. Appl.* **13** 165–72

[2] Breuer O and Sundararaj U 2004 Big returns from small fibers: a review of polymer/carbon nanotube composites *Polym. Compos.* **25** 630–41

[3] Phang I Y, Liu T, Zhang W D, Schonherr H and Vancso G J 2007 Probing buried carbon nanotubes within polymer–nanotube composite matrices by atomic force microscopy *Eur. Polym. J.* **43** 4136–42

[4] Staii C, Johnson A T and Pinto N J 2004 Quantitative analysis of scanning conductance microscopy *Nano Lett.* **4** 859–62

[5] Staii C, Pinto N J and Johnson A T 2004 Scanning conductance microscopy of carbon nanotubes and polyethylene oxide nanofibers *Am. Inst. Phys.* **723** 129–32

[6] Jespersen T S and Nygard J 2007 Mapping of individual carbon nanotubes in polymer/nanotube composites using electrostatic force microscopy *Appl. Phys. Lett.* **90** 183108

[7] Zhao M H, Gu X H, Lowther S E, Park C, Jean Y C and Nguyen T 2010 Subsurface characterization of carbon nanotubes in polymer composites via quantitative electric force microscopy *Nanotechnology* **21** 225702

[8] Leng Y and Williams C C 1994 Electrostatic characterization of biological and polymeric surfaces by electrostatic force microscopy *Colloids Surf.* A **93** 335–41

[9] Hu J, Xiao X D and Salmeron M 1995 Scanning polarization force microscopy—a technique for imaging liquids and weakly adsorbed layers *Appl. Phys. Lett.* **67** 476–8

[10] Xu L and Salmeron M 1998 Scanning polarization force microscopy study of the condensation and wetting properties of glycerol on mica *J. Phys. Chem.* B **102** 7210–5

[11] Denk W and Pohl D W 1991 Local electrical dissipation imaged by scanning force microscopy *Appl. Phys. Lett.* **59** 2171–3

[12] Garcia R and Perez R 2002 Dynamic atomic force microscopy methods *Surf. Sci. Rep.* **47** 197–301

[13] Martinez N F, Lozano J R, Herruzo E T, Garcia F, Richter C, Sulzbach T and Garcia R 2008 Bimodal atomic force microscopy imaging of isolated antibodies in air and liquids *Nanotechnology* **19** 384011

[14] Lozano J R and Garcia R 2009 Theory of phase spectroscopy in bimodal atomic force microscopy *Phys. Rev.* B **79** 014110

[15] Sader J E, Chon J W M and Mulvaney P 1999 Calibration of rectangular atomic force microscope cantilevers *Rev. Sci. Instrum.* **70** 3967–9

[16] Horcas I, Fernandez R, Gomez-Rodriguez J M, Colchero J, Gomez-Herrero J and Baro A M 2007 WSXM: a software for scanning probe microscopy and a tool for nanotechnology *Rev. Sci. Instrum.* **78** 013705

[17] Albonetti C, Casalini S, Borgatti F, Floreano L and Biscarini F 2011 Morphological and mechanical properties of alkanethiol self-assembled monolayers investigated via bimodal atomic force microscopy *Chem. Commun.* **47** 8823–5

[18] Baumann M and Stark R W 2010 Dual frequency atomic force microscopy on charged surfaces *Ultramicroscopy* **110** 578–81

[19] Martinez-Martin D, Herruzo E T, Dietz C, Gomez-Herrero J and Garcia R 2011 Noninvasive protein structural flexibility mapping by bimodal dynamic force microscopy *Phys. Rev. Lett.* **106** 4

[20] Rodriguez T R and Garcia R 2004 Compositional mapping of surfaces in atomic force microscopy by excitation of the second normal mode of the cantilever *Appl. Phys. Lett.* **84** 449–51

[21] Stark R W 2009 Dynamics of repulsive dual-frequency atomic force microscopy *Appl. Phys. Lett.* **94** 063109

[22] Xu L and Salmeron M 2001 Studies of wetting and capillary phenomena at nanometer scale with scanning polarization force microscopy *Nano-Surface Chemistry* ed M Rosoff (New York: Dekker) chapter 6, pp 243–87

[23] Melcher J, Kiracofe D, Hu S, Johnson S and Raman A 2012 *Virtual Environment for Dynamic AFM: Version 2.0 Comprehensive Manual* (NanoHub: Purdue University) (http://nanohub.org/resources/veda)

[24] Anczykowski B, Gotsmann B, Fuchs H, Cleveland J P and Elings V B 1999 How to measure energy dissipation in dynamic mode atomic force microscopy *Appl. Surf. Sci.* **140** 376–82

[25] Belaidi S, Girard P and Leveque G 1997 Electrostatic forces acting on the tip in atomic force microscopy: modelization and comparison with analytic expressions *J. Appl. Phys.* **81** 1023–30

[26] Halliday D, Resnick R and Walker J 1997 *Fundamentals of Physics Extended* 5th edn (New York: Wiley)

[27] Kim M H, Hong S M and Koo C M 2012 Electric actuation properties of SEBS/CB and SEBS/SWCNT nanocomposite films with different conductive fillers *Macromol. Res.* **20** 59–65

[28] Loppacher C, Bennewitz R, Pfeiffer O, Guggisberg M, Bammerlin M, Schar S, Barwich V, Baratoff A and Meyer E 2000 Experimental aspects of dissipation force microscopy *Phys. Rev.* B **62** 13674–9

[29] Zhu J, Brink M and McEuen P L 2008 Single-electron force readout of nanoparticle electrometers attached to carbon nanotubes *Nano Lett.* **8** 2399–404

[30] Jain A, Nair P R and Alam M A 2011 Strategies for dynamic soft-landing in capacitive microelectromechanical switches *Appl. Phys. Lett.* **98** 234104